

Quantum Monte Carlo impurity solver for cluster dynamical mean-field theory and electronic structure calculations with adjustable cluster base

Kristjan Haule

Department of Physics, Rutgers University, Piscataway, New Jersey 08854, USA

(Received 6 December 2006; revised manuscript received 11 February 2007; published 23 April 2007)

We generalized the recently introduced impurity solver [P. Werner *et al.*, Phys. Rev. Lett. **97**, 076405 (2006)] based on the diagrammatic expansion around the atomic limit and quantum Monte Carlo summation of the diagrams. We present generalization to the cluster of impurities, which is at the heart of the cluster dynamical mean-field methods, and to realistic multiplet structure of a correlated atom, which will allow a high-precision study of actinide and lanthanide based compounds with the combination of the dynamical mean-field theory and band-structure methods. The approach is applied to both the two-dimensional Hubbard and t - J models within cellular dynamical mean-field method. The efficient implementation of the algorithm, which we describe in detail, allows us to study coherence of the system at low temperature from the underdoped to overdoped regime. We show that the point of maximal superconducting transition temperature coincides with the point of maximum scattering rate, although this optimal doped point appears at different electron densities in the two models. The power of the method is further demonstrated in the example of the Kondo volume collapse transition in cerium. The valence histogram of the dynamical mean-field theory solution is presented, showing the importance of the multiplet splitting of the atomic states.

DOI: [10.1103/PhysRevB.75.155113](https://doi.org/10.1103/PhysRevB.75.155113)

PACS number(s): 71.27.+a, 71.30.+h

I. INTRODUCTION

One of the most active areas of condensed-matter theory is the development of new algorithms to simulate and predict the behavior of materials exhibiting strong correlations. Recent developments of the powerful many-body approach, the dynamical mean-field theory¹⁻³ (DMFT) and its cluster extensions,^{4,5} hold great promise in being able to accurately predict physical properties of this challenging class of materials. In recent years, the DMFT method has substantially advanced our understanding of the physics of the Mott transition and demonstrated its power to explain such problems as the structural phase diagrams of actinides,^{6,7} phonon response,⁸ optical conductivity,⁹ valence and x-ray absorption,¹⁰ and transport¹¹ of some of the archetype materials with strong correlations.

The success of the dynamical mean-field theory in the context of the electronic structure revitalized the search for fast and flexible impurity solvers which could treat Hund's coupling and spin-orbit coupling of the parent atomic constituents in the crystal environment of the lattice. Further, the newly developed cluster extensions of DMFT (Refs. 4 and 5) require faster impurity solver which could access low-temperature strong correlation limit.

Many impurity solvers were developed over the last few decades, including Hirsch-Fye quantum Monte Carlo method,¹² exact diagonalization,¹³ noncrossing approximation,¹⁴ and its extensions such as one-crossing approximation^{3,15} or SUNCA,¹⁶ iterative perturbation theory,¹⁷ Wilson's numerical renormalization-group¹⁸ expansion around the atomic limit,¹⁹ and many others.

Each method has some advantages and disadvantages, but at the present time, there is no method that works efficiently and produces accurate solutions for the Green's function in all regimes of parameters. Concentrating only on the most often employed method, numerically exact Hirsch-Fye quan-

tum Monte Carlo, the following weaknesses limit its usefulness in many realistic materials and clusters of strongly correlated models: (i) It cannot treat realistic multiplet structure, which is very important in strongly correlated f materials. (ii) The discretization of the imaginary time leads to considerable systematic error²⁰ and requires extrapolation to infinitesimally small time slices. (iii) The low-temperature regime in the strong correlation limit of large U is computationally very expensive, since it requires many time slices and infinite U models like t - J model are inaccessible.

All of the above-mentioned shortcomings of the conventional quantum Monte Carlo algorithm are eliminated by the continuous time quantum Monte Carlo method.²⁰⁻²³ In addition, this method is even much faster for most of the applications we tested (see, for example, Ref. 20), including cluster DMFT for the Hubbard model and application of local-density approximation (LDA)+DMFT to the actinides.

The basic idea and its implementation for the Hubbard model were recently published in Ref. 21. Further extensions to a more general impurity model was implemented in Ref. 22. The first demonstration of the power of our implementation was presented in Ref. 24 by a detailed low-temperature study of sodium-doped cobaltates and in Ref. 10 by a study of plutonium valence.

Here, we want to describe the powerful implementation of the method for applications to realistic materials with complicated multiplet structure, including all interaction terms: Hubbard U , Hund's coupling, and spin-orbit coupling. The extension to clusters of few sites and superconducting state within cluster DMFT will be addressed, and its power will be demonstrated by studying the low-temperature coherence of both the Hubbard and the t - J model. The Kondo volume collapse transition in elemental cerium will be re-examined, showing the valence histogram of the alpha and gamma phases of the material. More technical details of the implementation are given in the Appendix.

II. FORMALISM

In this section, we will explain the main steps of the recently developed quantum Monte Carlo method with emphasis on the generalization to clusters and multiplets of real materials.

The cluster dynamical mean-field approach can be conveniently expressed by the functional of the local Green's function³

$$\Gamma[G_{loc}] = \text{Tr} \log(G_0^{-1} - \Sigma) - \text{Tr}[\Sigma G] + \Phi[G_{loc}]. \quad (1)$$

Here, G_{loc} stands for the Green's function of the cluster or single site under consideration and is, in general, a matrix of the size equal to the number of sites times the number of correlated orbitals per site. Further, G_0 is the noninteracting Green's function $G_0^{-1} = \omega + \mu + \nabla^2 + V_{ext}$ and contains all quadratic terms of the Hamiltonian including periodic ionic potential of the crystal (V_{ext}). The interacting part of the functional $\Phi[G_{loc}]$ contains *all* two-particle irreducible skeleton diagrams inside the chosen cluster, i.e., $\Sigma = \delta\Phi[G_{loc}]/\delta G$.

Within the DMFT method, the summation of all the diagrams is achieved by solving the corresponding quantum impurity problem

$$Z = \int D[\psi^\dagger \psi] \exp \left[-S_c - \int_0^\beta d\tau \int_0^\beta d\tau' \sum_{\alpha\alpha'} \psi_{\alpha'}^\dagger(\tau) \Delta_{\alpha\alpha'}(\tau, \tau') \psi_{\alpha'}(\tau') \right], \quad (2)$$

where the Anderson impurity model hybridization Δ term plays the role of the generalized Weiss field that needs to be added to the cluster effective action S_c to obtain the local Green's function. The self-consistency condition which determines this Weiss field (hybridization Δ) is

$$G_{imp} = \frac{1}{\omega - E_{imp} - \Sigma - \Delta} = G_{loc} = \sum_{\mathbf{k}} \frac{1}{G_0^{-1}(\mathbf{k}) - \Sigma}. \quad (3)$$

In the general impurity problem defined in Eq. (2), the electrons in the cluster S_c hybridize with a matrix of Weiss fields $\Delta_{\alpha\beta}$. In the case of single-site DMFT for an f material, this hybridization is a 14×14 matrix, while in cluster DMFT for plaquette, it is an 8×8 matrix. In some cases, hybridization can be block diagonalized, as we will show in the Appendix below on the example of cellular DMFT for the normal state of the Hubbard model. However, in the superconducting state of the same model, the hybridization acquires off-diagonal components due to anomalous components of self-energy.

The cluster part of the action S_c can be very complicated, and the power of this method is that it can treat arbitrary interaction within the cluster. For real material study, the most important on-site terms are the Hund's couplings, which are usually expressed by the Slater integrals²⁵ (F_2, F_4 , and F_6 in case of f electrons). In addition, there is spin-orbit coupling $H_{SO} = \xi \mathbf{I} \cdot \mathbf{s}$ and crystal-field splittings as well as various hoppings and nonlocal interactions within the cluster.

The continuous time impurity solvers are based on the diagrammatic expansion of the partition function and sto-

chastic sampling of the diagrams. Two expansions were recently implemented: the expansion around the band limit²⁶ and the expansion in the hybridization strength.²¹ The latter seems to be superior in the strongly correlated regime due to a substantial reduction of the size of matrices that need to be manipulated,²⁰ and, most importantly, the empirical finding is that the minus sign problem in this approach is severely reduced or maybe even eliminated.^{20,22}

The expansion in hybridization strength has a long history starting with the famous noncrossing approximation¹⁴ and various extensions of it such as one crossing approximation (OCA),^{3,15} CTMA,²⁷ SUNCA.¹⁶ All these approximations can be viewed as partial summation of the same type of diagrams. With stochastic sampling, the summation of essentially all the diagrams is now possible. The only weakness of the approach is that it works exclusively with the imaginary time Green's functions and analytic continuation to real axis, and access to real axis self-energy, for example, is still hard to achieve. However, we believe that the substantially enhanced precision of the method, as compared to Hirsch-Fye quantum Monte Carlo (QMC), will make this step easier.

The idea of expanding partition function in terms of the hybridization with the conduction band dates back to the work of Yuval and Anderson.²⁸ In this work, mapping the hybridization expansion to Coulomb gas model leads to one of the first breakthroughs in the area of the Kondo problem. Generalization to asymmetric Anderson model was published by Haldane in Ref. 29. A similar approach was later used in exploring the physics of the generalized Hubbard model in the context of DMFT.³⁰ In this work, the hybridization expansion of the partition function was analyzed by renormalization-group analysis technique. An early implementation of the related idea to sum up the terms of the partition function by Monte Carlo sampling was implemented in Ref. 31 to solve the two two-channel Anderson impurity model.

A. Sampled partition function

In the continuous time quantum Monte Carlo method, the partition function is expanded in terms of hybridization strength Δ , and the resulting diagrams are summed up by stochastic Metropolis sampling. Taylor expansion of the impurity partition function [Eq. (2)] gives

$$Z = \int D[\psi^\dagger \psi] e^{-S_c} \sum_k \frac{1}{k!} \left[\sum_{\alpha\alpha'} \int_0^\beta d\tau \int_0^\beta d\tau' \psi_{\alpha'}(\tau') \times \psi_{\alpha'}^\dagger(\tau) \Delta_{\alpha\alpha'}(\tau, \tau') \right]^k, \quad (4)$$

and by separating the cluster contribution from the bath contribution, the partition function can be cast into the form

$$Z = \int D[\psi^\dagger \psi] e^{-S_c} \sum_k \frac{1}{k!} \int_0^\beta \prod_{i=1}^k d\tau_i \int_0^\beta \prod_{i=1}^k d\tau'_i \times \sum_{\alpha\alpha'} \prod_{i=1}^k [\psi_{\alpha'_i}(\tau'_i) \psi_{\alpha_i}^\dagger(\tau_i)] \prod_{i=1}^k \Delta_{\alpha_i \alpha'_i}(\tau_i, \tau'_i). \quad (5)$$

It becomes clear that the partition function is a product of two terms: the average over the cluster states ψ and the average over the bath degrees of freedom Δ . It was pointed out in Ref. 21 that naive sampling of the above diagrams would run into a very bad minus sign problem. The reason is that crossing diagrams (vertex corrections to famous noncrossing

approximation to the Anderson impurity model) can have either sign, and thus weights that correspond to crossing diagrams could be negative. The ingenious idea proposed in Ref. 21 is to combine all the diagrams of the same order, crossing and noncrossing, into a determinant. Mathematically, this can be expressed by

$$\begin{aligned}
 Z = Z_c \sum_k \frac{1}{k!} \int_0^\beta d\tau_1 \int_0^\beta d\tau'_1 \cdots \int_0^\beta d\tau_k \int_0^\beta d\tau'_k \sum_{\alpha_1, \alpha'_1, \dots, \alpha_k, \alpha'_k} \langle T_\tau \psi_{\alpha'_1}(\tau'_1) \psi_{\alpha_1}^\dagger(\tau_1) \cdots \psi_{\alpha'_k}(\tau'_k) \psi_{\alpha_k}^\dagger(\tau_k) \rangle_{cluster} \\
 \times \frac{1}{k!} \det \begin{pmatrix} \Delta_{\alpha_1 \alpha'_1}(\tau_1, \tau'_1) & \Delta_{\alpha_1 \alpha'_2}(\tau_1, \tau'_2) & \cdots & \cdots \\ \cdots & \cdots & \cdots & \cdots \\ \cdots & \cdots & \cdots & \cdots \\ \Delta_{\alpha_k \alpha'_1}(\tau_k, \tau'_1) & \cdots & \cdots & \Delta_{\alpha_k \alpha'_k}(\tau_k, \tau'_k) \end{pmatrix}, \quad (6)
 \end{aligned}$$

where $Z_c = \int D[\psi^\dagger \psi] e^{-S_c}$ and the average of the operator is $\langle O \rangle_{cluster} = \frac{1}{Z_c} \int D[\psi^\dagger \psi] e^{-S_c} O$. This is the central equation of the continuous time Monte Carlo sampling around the atomic limit. To derive Eq. (6) from Eq. (5), one needs to permute time integration variables τ in all possible ways. Permutation of fermions gives minus sign in an odd permutation. This minus sign can be absorbed in the minus sign of the product of hybridizations, resulting in the determinant of hybridizations.

B. Simulation

The set of diagrams, which are associated with the set of imaginary times $\{\tau_1, \tau'_1, \tau_2, \tau'_2, \dots, \tau_k, \tau'_k\}$ and corresponding band indices $\{\alpha_1, \alpha'_1, \alpha_2, \alpha'_2, \dots, \alpha_k, \alpha'_k\}$, are visited by the Monte Carlo (Metropolis) algorithm with the weights given by Eq. (6). The effect of the hybridization $\psi(\tau') \psi^\dagger(\tau) \Delta(\tau - \tau')$ is to create a kink in the time evolution of the cluster, i.e., to destroy one electron at time τ' on the cluster and create another electron at some other time τ on the cluster. The number of kinks is always even due to particle number conservation.

Two Monte Carlo steps which need to be implemented are (i) insertion of two kinks at random times τ_{new} and τ'_{new} (chosen uniformly $[0, \beta)$), corresponding to random baths α and α' , and (ii) removal of two kinks by removing one creation operator and one annihilation operator. Many other steps can greatly reduce the sampling time, for example, displacing a randomly chosen operator (either ψ or ψ^\dagger) to a new location chosen uniformly $[0, \beta)$. The double step of inserting or removing two kinks is also possible and is relevant when off-diagonal components of Δ are dominant.

The detailed balance condition requires that the probability to insert two kinks at random times τ and τ' , being chosen uniformly in the interval $[0, \beta)$, is

$$P_{add} = \min \left[\left(\frac{\beta N_b}{k+1} \right)^2 \frac{\mathcal{Z}_{new} \mathcal{D}_{new}}{\mathcal{Z}_{old} \mathcal{D}_{old}}, 1 \right], \quad (7)$$

where N_b is the number of baths, k is the current perturbation order (number of kinks/2), \mathcal{Z}_{new} is the cluster matrix element,

$$\begin{aligned}
 \mathcal{Z}_{new} = \langle T_\tau \psi_{\alpha'_1}(\tau'_1) \psi_{\alpha_1}^\dagger(\tau_1) \cdots \psi_{\alpha'_k}(\tau'_k) \psi_{\alpha_k}^\dagger(\tau_k) \rangle_{cluster}, \quad (8) \\
 \times \psi_{\alpha'_1}(\tau_1) \cdots \psi_{\alpha'_k}(\tau_k) \psi_{\alpha_k}^\dagger(\tau_k) \psi_{\alpha_1}^\dagger(\tau_1)
 \end{aligned}$$

and $\mathcal{D}_{new}/\mathcal{D}_{old}$ is the ratio between the new and the old determinant of baths Δ and can be evaluated using usual Sherman-Morrison formulas. The factors (βN_b) enter because of the increase of the phase space when adding kinks (increase of entropy), while the factor $1/(k+1)$ comes from factorials in Eq. (6). Similarly, the probability to remove two kinks, chosen randomly between $[1 \cdots k]$, is

$$P_{remove} = \min \left[\left(\frac{k}{\beta N_b} \right)^2 \frac{\mathcal{Z}_{new} \mathcal{D}_{new}}{\mathcal{Z}_{old} \mathcal{D}_{old}}, 1 \right]. \quad (9)$$

An important simplification occurs if the hybridization is block diagonal. Since $\Delta_{\alpha\alpha'}$ vanishes for some combination of $\alpha\alpha'$, the determinant in Eq. (6) can be written as a product of smaller determinants, one for each block of hybridization. A specially simple case occurs when all the blocks are of size 1, and the partition function becomes a product of N_b terms, where N_b is the number of all baths,

$$\begin{aligned}
Z = Z_c \sum_{\{k_\alpha\}} \frac{1}{k_\alpha!} \int_0^\beta \prod_{\alpha=1}^{N_b} \prod_{i=1}^{k_\alpha} d\tau_i^\alpha \int_0^\beta \prod_{\alpha=1}^{N_b} \prod_{i=1}^{k_\alpha} d\tau_i^{\prime\alpha} \left\langle T_\tau \prod_\alpha \psi_\alpha(\tau_i^\alpha) \psi_\alpha^\dagger(\tau_i^\alpha) \cdots \psi_\alpha(\tau_{k_\alpha}^{\prime\alpha}) \psi_\alpha^\dagger(\tau_{k_\alpha}^{\prime\alpha}) \right\rangle_{cluster} \\
\times \prod_\alpha \frac{1}{k_\alpha!} \det \begin{pmatrix} \Delta_\alpha(\tau_1^\alpha, \tau_1^{\prime\alpha}) & \Delta_\alpha(\tau_1^\alpha, \tau_2^{\prime\alpha}) & \cdots \\ \cdots & \cdots & \cdots \\ \cdots & \cdots & \cdots \\ \Delta_\alpha(\tau_{k_\alpha}^\alpha, \tau_{k_\alpha}^{\prime\alpha}) & \cdots & \Delta_\alpha(\tau_{k_\alpha}^\alpha, \tau_{k_\alpha}^{\prime\alpha}) \end{pmatrix}. \quad (10)
\end{aligned}$$

This simplified form of Eq. (6) was first derived in Ref. 22. In this case, the probability to add two new kinks [Eq. (7)] depends on the number of kinks of this particular type k_α (rather than the total perturbation order k), and the dimension of the bath subspace N_b becomes unity. In general, the probability to add two kinks is $P_{add} = \left(\frac{\beta N_b}{k_\alpha + 1}\right)^2 \frac{Z_{new} D_{new}^\alpha}{Z_{old} D_{old}^\alpha}$, where N_b^α is the number of bands which form an off-diagonal subblock in hybridization Δ and need to be treated simultaneously in one determinant D^α in Eq. (6).

The size of hybridization determinants can thus be greatly reduced if hybridization Δ is block diagonal. The cluster term Z , however, cannot be broken into separate contributions for each bath; rather, the full trace needs to be computed numerically. It is therefore essential to find a fast way to compute the cluster average $\langle \cdots \rangle_{cluster}$ in Eq. (6).

C. Exact diagonalization of the cluster

As noted in Refs. 3 and 22, the perturbation theory in hybridization strength requires the cluster Hamiltonian to be converted to a quadratic form, which can be achieved with the introduction of the cluster eigenstates and projectors to the eigenstates. In terms of Hubbard operators $X_{mm'}$ (or equivalently pseudoparticles $a_m^\dagger a_{m'}$), the cluster Hamiltonian simplifies to $H_{cluster} = X_{mm} E_m$ and the cluster traces can be efficiently computed. It is also crucial to take into account the conservation of various quantum numbers, such as the particle number, the total spin, and the total momentum of the cluster states, when evaluating the cluster traces.

Typical contribution to the cluster part of the trace that needs to be evaluated at each Monte Carlo step takes the form

$$\begin{aligned}
Z_D = \text{Tr} \left(T_\tau \exp \left[- \int_0^\beta d\tau H_c(\tau) \right] \psi_{\alpha_1}(\tau_1') \right. \\
\left. \times \psi_{\alpha_2}^\dagger(\tau_2) \cdots \psi_{\alpha_{n-1}}(\tau_{n-1}') \psi_{\alpha_n}^\dagger(\tau_n) \right) \\
= \sum_{\{m\}} e^{-E_{m_1} \tau_1'} (F^{\alpha_1})_{m_1 m_2} e^{-E_{m_2} (\tau_2 - \tau_1')} \\
\times (F^{\dagger \alpha_2})_{m_2 m_3} \cdots (F^{\alpha_{n-1}})_{m_{n-1} m_n} e^{-E_{m_n} (\tau_{n-1}' - \tau_n)} \\
\times (F^{\dagger \alpha_n})_{m_n m_1} e^{-E_{m_1} (\beta - \tau_n)}, \quad (11)
\end{aligned}$$

where the matrix elements are $(F^{\dagger \alpha_i})_{nm} = \langle n | \psi_{\alpha_i}^\dagger | m \rangle$ and E_m are

eigenvalues of the cluster. The actual order of operators in Eq. (11) depends on their time arguments, and creation operator is not necessary followed by annihilation operator.

The bottleneck of the approach is that the number of cluster states $|m\rangle$ is very large (for example, single-site DMFT for the f shell requires 2^{14} states). Consequently, the matrix elements F are, in general, very large matrices and the typical diagram order is inversely proportional to temperature (see Fig. 1); therefore, one typically needs to multiply a few hundred large matrices at each Monte Carlo step. It is clear that this is very impractical, and the progress can be achieved only by the following various tricks which we have implemented:

- (1) Most of the matrix elements vanish. A fast algorithm is needed to determine which matrix elements are nonzero.
- (2) Symmetries of the problem can be taken into account to reduce the size of the F matrix.
- (3) The number of trial steps is usually much bigger (100 times) than the number of accepted steps, and the insertion or removal of a kink is very local in time operation. It is convenient to store the product [Eq. (11)] (from both sides, left and right), and when trying to insert a new kink, recompute the trace only between the inserted times τ_{new} and τ'_{new} .
- (4) During simulation, the probability for visiting any cluster state can be recorded and can be used in the next step

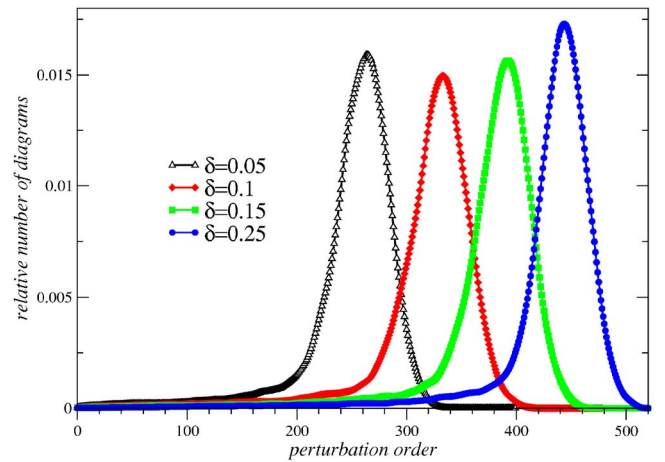


FIG. 1. (Color online) The perturbation order histogram shows the distribution of the typical perturbation order of the diagrams in the simulation. The histogram is peaked around the typical order, which is related to temperature and kinetic energy by $\langle k \rangle = |E_{kin}|/T$.

to eliminate the irrelevant atomic states from the trace in Eq. (11). The cluster base can hence be adjusted dynamically to describe the particular regime studied by the minimum number of relevant cluster states.

To illustrate the method, let us consider a concrete example of the cluster of one-band model (Hubbard or t - J) in the normal state. The bath index α runs over cluster momenta \mathbf{q} and spin orientation σ . The eigenstates of the cluster can be written in a form $|N, S_z, \mathbf{K}; S\gamma\rangle$, where N is the total number of electrons in the state, S and S_z are the total spin and its z components, \mathbf{K} is the total momentum of the cluster state, and γ stands for the rest of the quantum numbers.

D. Concept of superstates

In this base, the matrix elements of the creation operator are greatly simplified, $\psi_{\mathbf{q},\sigma}^\dagger |N, S_z, \mathbf{K}; S\gamma\rangle = |N+1, S_z + \sigma, \mathbf{K} + \mathbf{q}; S \pm 1/2, \gamma\rangle$, because the creation operator is nonzero only between Hilbert subspace of $\{N, S_z, \mathbf{K}\}$ and $\{N+1, S_z + \sigma, \mathbf{K} + \mathbf{q}\}$. It is therefore convenient to group together states with the same $\{N, S_z, \mathbf{K}\}$ and treat the rest of the quantum numbers as internal degrees of freedom of a cluster superstate $|i\rangle \equiv |\{N, S_z, \mathbf{K}\}\rangle$. The superstate $|i\rangle$ is a multidimensional state with internal quantum numbers $|m[i]\rangle \equiv |\{S, \gamma\}\rangle$. It is then clear that creation operator acting on a state $|i\rangle$ gives a unique state $|j\rangle = \psi_{\mathbf{q},\sigma}^\dagger |i\rangle$, and it is enough to store a single index array $F^{\alpha\dagger}(i) = j$ to figure out how the Hilbert subspaces are visited under application of a sequence of creation and annihilation operators such as in Eq. (11): $i_0 \rightarrow F^{\alpha_1}(i_0) \rightarrow \dots \rightarrow i_k = F^{\alpha_k}(i_{k-1})$. This sequence is very often truncated in few steps only because most of the sequences contain either multiple application of the same creation or annihilation operator (Pauli principle) or because they lead to a state outside the base (for example, $\psi|N=0\dots\rangle=0$ or $\psi^\dagger|N=\max\dots\rangle=0$).

Once the nonzero matrix elements are found by this simple index lookup, the value of the matrix element needs to be computed by matrix multiplication. By this breakup of the Hilbert space and introducing superstates $|i\rangle$, the largest matrix which needs to be treated for the t - J model on a plaquette is 3×3 and for the Hubbard model it is 6×12 , thus substantially smaller than the original 81- and 265-dimensional Hilbert spaces. To compute the trace in Eq. (11), we start with unity matrix in each subspace of a superstate $|i\rangle$ and apply both the time evolution operator $e^{-E_m(\tau-\tau')}$ (by multiplying each row of a matrix with its time evolution) and the kink [by multiplication with the matrix $(F^\alpha)_{mn}$ or $(F^{\alpha\dagger})_{mn}$]. The operation of F brings us to the next superstate $F^\alpha(i)$ where we repeat both the time evolution and the kink application. After k steps, the trace of a matrix gives the desired matrix element.

E. Storing the time evolution

The number of kinks is proportional to inverse temperature β and kinetic energy of the system $\langle k \rangle = \beta |E_{kin}|$ [see Eq. (47)]. It thus becomes large at low temperatures. However, an insertion of a kink with large time difference $[\psi^\dagger(\tau)\psi(\tau')$ with large $\tau - \tau'$] has a very low probability. The reason is

that Pauli principle forbids insertion of the pair $\psi_\alpha^\dagger(\tau)\psi_\alpha(\tau')$ if another kink of the same species α is between the two times (τ, τ') . At the same time, $\Delta(\tau)$ is like $G(\tau)$ peaked at small times $\tau - \tau'$ and falls off at large times, making the long time intervals rare.

The insertion of a kink is thus fairly local in time operation; therefore, it is convenient to store a whole chain of products that appear in Eq. (11) from both sides, left and right, to make trial step very cheap. It takes only few matrix multiplications (almost independent of temperature) to compute the trace in Eq. (11). When the move is accepted, the trace needs to be updated, which takes somewhat more time. However, the acceptance rate is typically small and, on average, does not require much computational time.

F. Adjusting the cluster base

Finally, the ultimate speedup can be achieved by dynamically adjusting “the best” cluster base. The probability for a cluster state $|m\rangle$ can be computed during simulation. For a given diagram with particular configuration of kinks, the probability for a cluster state $|m\rangle$ is proportional to its matrix element defined in Eq. (11), i.e.,

$$P_m = \frac{\langle m | e^{-H\tau_1} \psi_\alpha e^{-H(\tau_2-\tau_1)} \dots | m \rangle}{\sum_{\{n\}} \langle n | e^{-H\tau_1} \psi_\alpha e^{-H(\tau_2-\tau_1)} \dots | n \rangle}. \quad (12)$$

The sampled average of this quantity gives the probability for cluster eigenstate $|m\rangle$. A large number of cluster states have very small probability and can be eliminated in simulation to ultimately speed up the simulation. It is important that the probability for any cluster state depend on the particular problem at hand and the program adjust the base dynamically after a few million Monte Carlo steps.

G. Green's function evaluation

Like in other impurity solvers which are based on the expansion of the hybridization [noncrossing approximation (NCA), OCA, and SUNCA], the Green's function is computed from the bath electron T matrix. Using the equation of motion, it is easy to see that the bath Green's function $G_{kk'}$ is connected to the local Green's function G_{loc} through the following identity:

$$G_{kk'}(\tau - \tau') = \delta_{kk'} g_{kk}(\tau - \tau') + \int_0^\beta \int_0^\beta d\tau_s d\tau_e g_k(\tau - \tau_e) \times V_k G_{loc}(\tau_e - \tau_s) V_{k'} g_{k'}(\tau_s - \tau'), \quad (13)$$

or summing over momenta

$$\begin{aligned} \mathcal{G}(\tau - \tau') &\equiv \sum_{kk'} V_k G_{kk'}(\tau - \tau') V_{k'} \\ &= \Delta(\tau - \tau') + \int_0^\beta \int_0^\beta d\tau_s d\tau_e \Delta(\tau - \tau_e) \\ &\quad \times G_{loc}(\tau_e - \tau_s) \Delta(\tau_s - \tau'). \end{aligned} \quad (14)$$

This Green's function \mathcal{G} is equal to the ratio between the determinant of Δ 's,

$$\mathcal{G}(\tau - \tau') = \frac{\det \left(\begin{array}{c|ccc} \Delta(\tau, \tau') & \Delta(\tau, \tau'_1) & \cdots & \\ \Delta(\tau_1, \tau') & & & \\ \vdots & & & \\ \Delta(\tau_k, \tau') & & & \underline{\Delta} \end{array} \right)}{\det(\underline{\Delta})},$$

where one row and one column is added to the bath electron determinant. The reason for this simple form is that the conduction band is noninteracting and thus obeys Wicks theorem. Here, we used the definition

$$\underline{\Delta} \equiv M^{-1} = \begin{pmatrix} \Delta_\alpha(\tau_1^\alpha, \tau'_1) & \cdots & \\ \cdots & \cdots & \\ \cdots & \Delta_\alpha(\tau_{k_\alpha}^\alpha, \tau'_{k_\alpha}) & \end{pmatrix}, \quad (15)$$

Using the Sherman-Morrison formulas to express enlarged determinant by the original determinant of $\underline{\Delta}$, \mathcal{G} becomes

$$\mathcal{G}(\tau - \tau') = \Delta(\tau - \tau') - \sum_{i_e, i_s} \Delta(\tau - \tau_{i_e}) M_{i_e, i_s} \Delta(\tau_{i_s} - \tau'). \quad (16)$$

Finally, comparing Eqs. (14) and (16), we see that $G_{loc}(\tau_e - \tau_s) = -M_{i_e, i_s}$, and in imaginary frequency,

$$G_{loc}(i\omega) = -\frac{1}{\beta} \sum_{i_e, i_s} e^{i\omega\tau_{i_e}} M_{i_e, i_s} e^{-i\omega\tau_{i_s}}. \quad (17)$$

This equation is the central equation of the approach, since it relates the local Green's function with the quantities computed in QMC importance sampling. This equation is equivalent to the well-known formulas used in the perturbation theory in hybridization strength, namely, that the local Green's function is proportional to the conduction-electron self-energy. Equation (17) shows that only matrix $M \equiv (\underline{\Delta})^{-1}$ needs to be stored²¹ and manipulated in simulation.

From the above consideration, it is clear that one could also add two rows and two columns to matrix $\underline{\Delta}$ and compute the two-particle vertex function in a similar way without much overhead.

H. Fast updates

The Green's function can be updated in linear time (rather than quadratic). When adding a construction and annihilation operator at τ and τ' , adding a column at i_s and row at i_e to matrix M^{-1} leads to the following relation between the matrix M_{new} and M_{old} :

$$M_{ji}^{new} = M_{ji}^{old} + pL_j R_i. \quad (18)$$

Here, one row and one column of zeros is added to M^{old} to match the size of M^{new} . The arrays L and R are given by

$$L = (\tilde{L}_1, \dots, \tilde{L}_{i_e-1}, -1, \dots, \tilde{L}_k), \quad (19)$$

$$R = (\tilde{R}_1, \dots, \tilde{R}_{i_s-1}, -1, \dots, \tilde{R}_k), \quad (20)$$

where

$$\tilde{L}_j = \sum_i M_{ji}^{old} \Delta(\tau_i - \tau'), \quad (21)$$

$$\tilde{R}_i = \sum_j \Delta(\tau - \tau_j) M_{ji}^{old}, \quad (22)$$

and p is

$$\frac{1}{p} = \Delta(\tau - \tau') - \sum_{ij} \Delta(\tau - \tau_j) M_{ji}^{old} \Delta(\tau_i - \tau'). \quad (23)$$

Finally, the local Green's function becomes

$$G^{new} = G^{old} - \frac{p}{\beta} \left(\sum_{j_e} e^{i\omega\tau_{j_e}} L_{j_e} \right) \left(\sum_{j_s} R_{j_s} e^{-i\omega\tau_{j_s}} \right). \quad (24)$$

It is clear from Eq. (24) that only linear amount of time is needed to update the local Green's function.

When removing two kinks of construction and annihilation operators at i_s and i_e , old and new matrices M are related by

$$M_{ij}^{new} = M_{ij}^{old} - \frac{M_{i_s}^{old} M_{i_e}^{old}}{M_{i_e, i_s}^{old}}. \quad (25)$$

Green's function therefore becomes

$$G^{new} = G^{old} + \frac{1}{\beta M_{i_e, i_s}^{old}} \left(\sum_{j_e} e^{i\omega\tau_{j_e}} M_{j_e, i_s} \right) \left(\sum_{j_s} M_{i_e, j_s} e^{-i\omega\tau_{j_s}} \right). \quad (26)$$

Finally, the exponential factors $e^{i\omega\tau_i}$ do not need to be recomputed at each Monte Carlo step since all "old" times can be stored and the exponents need to be computed only for the new pair of times and only at each accepted move. In the present implementation, the algorithm to sample directly $G(i\omega)$ is sufficiently fast that it does not introduce any performance costs. Since it does not introduce systematic error in binning $G(\tau)$ we believe that it is more superior than the alternative implementations which sample $G(\tau)$.

I. Large frequencies and moments

Similar to the Hirsch-Fye QMC, the low-frequency points of Green's function converge very fast to the exact value while the high-frequency points, when sampled directly, contain a lot of noise. It is therefore not very useful to sample large frequencies in the above described way. Usually, we sample 200–300 Matsubara points while the rest are replaced by the high-frequency moments of the self-energy computed analytically.

The high-frequency moments of the self-energy are computed from the Green's function moments, which, in general, take the following form:

$$m_n^{\alpha\beta} = (-1)^n \langle \{ [H, [H, \dots [H, \psi_\alpha] \dots]], \psi_\beta^\dagger \} \rangle. \quad (27)$$

To compute the moments within the present approach, few operators need to be sampled in simulation. In the one-band model, only density is required, but in more complicated situation, higher-order density-density and exchange terms

enter. In general, Green's function moments can be expressed by the average of a few equal-time operators $O_{mm'}$, which take particular simple form in the local eigenbase,

$$m_{1,mm'}^{G,\alpha\beta} = \sum_n (F^\alpha)_{mn} (F^{\beta\dagger})_{nm'} (E_n - E_m) - (F^{\beta\dagger})_{mn} (F^\alpha)_{nm'} (E_n - E_{m'}), \quad (28)$$

$$m_{2,mm'}^{G,\alpha\beta} = \sum_n (F^\alpha)_{mn} (F^{\beta\dagger})_{nm'} (E_m - E_n)^2 + (F^{\beta\dagger})_{mn} (F^\alpha)_{nm'} (E_n - E_{m'})^2. \quad (29)$$

The lowest-order self-energy moments can then be computed in the following way:

$$\Sigma_{\alpha\beta}(\infty) = \langle m_1^{G,\alpha\beta} \rangle - E_{imp}, \quad (30)$$

$$\Sigma_{\alpha\beta}^{(1)} = \langle m_2^{G,\alpha\beta} \rangle - \langle m_1^{G,\alpha\beta} \rangle^2. \quad (31)$$

J. Sampling of other quantities

Equal-time operators such as those in Eqs. (28) and (29) can be straightforwardly computed in simulation. Any cluster operator can be expressed in terms of Hubbard operators $X_{mm'}$, which project to the cluster eigenbase, and matrix elements of the operator in the cluster eigenbase as follows:

$$O = \langle m|O|m' \rangle X_{mm'}. \quad (32)$$

To compute the expectation value of the operator, the following probabilities are needed:

$$P_{mm'} \equiv \langle X_{mm'} \rangle. \quad (33)$$

Diagonal components are just cluster probabilities [Eq. (12)], while the off-diagonal components are transition probabilities from cluster eigenstate $|m\rangle$ to $|m'\rangle$. The expectation value of any cluster operator is then given by

$$\langle O \rangle = \sum_{mm'} \langle m|O|m' \rangle P_{mm'}. \quad (34)$$

To improve the sampling precision, operators are averaged over all times, i.e.,

$$P_{mm'} = \frac{1}{\beta} \int_0^\beta \langle X_{mm'}(\tau_0) \rangle d\tau_0 = \frac{1}{Z} \frac{1}{\beta} \int_0^\beta d\tau_0 \text{Tr} \left[T_\tau \exp \left(- \int_0^{\tau_0} H d\tau \right) \times X_{mm'}(\tau_0) \exp \left(- \int_{\tau_0}^\beta H d\tau \right) \right]. \quad (35)$$

The contribution to $P_{mm'}$ of each particular diagram is

$$\frac{1}{Z_{\mathcal{D}}} \sum_{n,l=1}^{l=k} (T_l^{left})_{nm} w_{mm'}(\tau_{l+1}, \tau_l) (T_{k-l}^{right})_{m'n}, \quad (36)$$

where

$$w_{mm'}(\tau_{l+1}, \tau_l) = \int_{\tau_l}^{\tau_{l+1}} \frac{d\tau}{\beta} e^{-E_m(\tau-\tau_l) - E_{m'}(\tau_{l+1}-\tau)}, \quad (37)$$

$Z_{\mathcal{D}}$ is the cluster part of the trace [Eq. (11)], T_l^{left} are the operators in Eq. (11) which appear before τ , and T_{k-l}^{right} contains operator with time arguments greater than τ . k is the number of kinks in the diagram \mathcal{D} . As we mentioned before, these time evolution operators (T_l^{left}, T_l^{right}) are stored and regularly updated during simulation.

The weights [Eq. (37)] evaluate to

$$w_{mm'}(\Delta\tau) = \frac{e^{-E_m\Delta\tau} - e^{-E_{m'}\Delta\tau}}{\beta(E_{m'} - E_m)}. \quad (38)$$

For the diagonal probabilities P_{mm} and for degenerate cluster states ($E_m = E_{m'}$), the weights are simplified to

$$w_{mm'}(\Delta\tau) = e^{-E_m\Delta\tau} \frac{\Delta\tau}{\beta}. \quad (39)$$

Further simplification is possible if operator $\langle O \rangle$ commutes with $H_{cluster}$ because only the diagonal probabilities P_{mm} are needed in this case. For example, the electron density n_f and average magnetization $\langle S_z \rangle$ are two important quantities which can be computed to very high precision in this way.

Similar simplification is possible in the case of the total spin susceptibility, defined by

$$\chi(i\omega) = \frac{1}{\beta} \int_0^\beta d\tau \int_0^\beta d\tau' \langle S_z(\tau) S_z(\tau') \rangle e^{i\omega(\tau-\tau')}, \quad (40)$$

where S_z is the total spin of the cluster (or atom). The result is

$$\chi(i\omega) = \sum_{i \in \text{superstates}} P_i \left| \sum_{l=1}^k (S_z)_{j_l} \frac{e^{i\omega\tau_{l+1}} - e^{i\omega\tau_l}}{i\omega} \right|^2, \quad (41)$$

where $(S_z)_{j_l}$ is the total spin of the cluster in cluster eigenstate j and P_i is a probability for a superstate $|i\rangle$, introduced above.

If one of the bands in the multiorbital band model is fully filled or completely empty, the Anderson impurity bath is very weakly coupled to the impurity. To compute the local Green's function from the conduction bath self-energy [see Eq. (13)] becomes a numerically very challenging task. In this situation, it is numerically more stable to compute the local Green's function directly from the cluster trace. Expressing electron operators in terms of the Hubbard operators, the local Green's function becomes

$$G_{\alpha\beta}(i\omega) = \sum_{m'n'm'} (F^\alpha)_{mn} (F^{\beta\dagger})_{n'm'} \frac{1}{\beta} \int_0^\beta d\tau \int_0^\beta d\tau' e^{i\omega(\tau-\tau')} \times \langle T_\tau X_{mn}(\tau) X_{n'm'}(\tau') \rangle. \quad (42)$$

For each diagram \mathcal{D} visited in Monte Carlo sampling, the following quantity can be sampled for the Green's function:

$$G_{\alpha\beta}^D = T \sum_{mnm'm'p_l l_2} (F^\alpha)_{mn} (F^{\beta\dagger})_{n'm'} (T_{0,l_1})_{pm} e^{i\omega\tau_1} w_{mn}(i\omega, \Delta\tau_{l_1}) \\ \times (T_{l_1,l_2})_{nm'} w_{m'n'}(i\omega, \Delta\tau_{l_2}) e^{-i\omega\tau_{l_2+1}} (T_{l_2,k})_{m'p}, \quad (43)$$

where

$$w_{mn}(i\omega, \Delta\tau) = \frac{e^{-E_n\Delta\tau} - e^{(i\omega - E_m)\Delta\tau}}{i\omega - E_m + E_n}$$

and $\Delta\tau_l = \tau_{l+1} - \tau_l$. This expression is most valuable in the limit of a small number of kinks in an orbital, which results in a numerically unstable computation of Green's function when using Eq. (17).

K. Sampling the total energy

The average of the potential energy $\langle V \rangle$ can be computed from the average of the local energy since

$$\langle H_{loc} \rangle = \sum_{\alpha\beta\gamma\delta} U_{\alpha\beta\gamma\delta} \langle \psi_\alpha^\dagger \psi_\beta^\dagger \psi_\gamma \psi_\delta \rangle + \sum_{\alpha\beta} E_{imp\alpha\beta} \langle \psi_\alpha^\dagger \psi_\beta \rangle \\ = \langle V \rangle + \text{Tr}[E_{imp}n]. \quad (44)$$

Here, we concentrate on the case of general single-site DMFT rather than the cluster extensions. The reason is that kinetic energy in cluster extensions depends on the periodization scheme and we will not go into detail here. The kinetic energy of the general single-site DMFT $E_{kin} = \text{Tr}[H_{\mathbf{k}}^0 G_{\mathbf{k}}]$ can be computed by

$$E_{kin} = \text{Tr}[\Delta G] + \text{Tr}[(\mu + E_{imp})n]. \quad (45)$$

The total energy is therefore given by

$$\langle H \rangle = \langle H_{loc} \rangle + \text{Tr}[\Delta G] + \mu n. \quad (46)$$

The first term H_{loc} can be computed very precisely in simulation. The sampled quantity $\langle O \rangle$ is just the energy of an atomic state and can be simply obtained from the probabilities for atomic states $\langle H_{loc} \rangle = \sum_{m \in \text{all states}} P_m E_m$. Computing kinetic energy from the Green's function gives, in general, worse accuracy because the high-frequency behavior of the Green's function cannot be directly sampled and augmentation with analytically computed tails is necessary. However, it is simple to show that the average value of the perturbation order is related to the average of the kinetic energy as follows:

$$\langle k \rangle = -\frac{1}{T} \text{Tr}[\Delta G], \quad (47)$$

where $\langle k \rangle$ is the average perturbation order and T is temperature. The latter quantity is directly sampled in the present algorithm and it is just the center of gravity of the histogram (presented in Fig. 1). Finally, the total energy E is given by

$$E_{tot} = \langle H_{local} \rangle - T \langle k \rangle + \mu n. \quad (48)$$

All quantities in this equation can be computed to very high accuracy, and since low temperatures can be reached in this method, the entropy can be obtained by integrating the specific heat as shown in Ref. 23.

L. Superconductivity

The power of the method can be further demonstrated by studying the superconducting state of the strongly correlated systems at low temperature with essentially no performance cost. By employing the Nambu formalism, the translationally invariant cluster methods (for details on cellular DMFT on a plaquette, see the Appendix) result in N_c two-dimensional baths, where N_c is the number of cluster momenta. Namely, the baths $\{\mathbf{K}, \uparrow\}$ and $\{-\mathbf{K}, \downarrow\}$ are coupled through the anomalous component of hybridization and require simultaneous treatment in $\det(\underline{\Delta})$ in Eq. (10). The determinants are, on average, twice as large as in normal state; however, the cluster part of the trace in Eq. (10) remains unchanged. Since most of the time is usually spent in evaluating the local part of Z , the performance is not noticeably degraded in superconducting state. In a typical run presented below, the histogram is peaked around $k=250-500$, which is equal to the order of a typical diagram. In the translationally invariant representation employed here, the size of a typical determinant in Eq. (10) is only $k/N_c \sim 60-120$, and using the fast-update scheme presented above, the trace over the bath states is not the expensive part of the algorithm.

M. Hund's coupling and spin-orbit coupling

In materials with open f orbitals, the multiplet effects are very strong and $SU(N)$ approximation is not adequate. Simultaneous inclusion of Hund's coupling and spin-orbit coupling in DMFT method is crucial for a quantitative description of actinides.¹⁰ The minimal local Hamiltonian for lanthanide and actinide materials is

$$H_{atom} = H_{Hubbard+Hunds} + H_{SO} + \tilde{E}_{imp}\hat{n}. \quad (49)$$

Here, \tilde{E}_{imp} is the impurity level without the spin-orbit coupling since the latter is included explicitly. The Hund's coupling and spin-orbit coupling take the following forms:

$$H_{Hubbard+Hunds} = \sum_{L_i, m, \sigma\sigma'} \sum_{k=0}^{2l} \frac{4\pi F_{\{l\}}^k}{2k+1} \langle Y_{L_a} | Y_{k m} | Y_{L_c} \rangle \\ \times \langle Y_{L_d} | Y_{k m} | Y_{L_b} \rangle f_{L_a}^\dagger \alpha f_{L_b}^\dagger \sigma' f_{L_d} \sigma' f_{L_c} \sigma, \quad (50)$$

$$H_{SO} = \sum_{jm_j, lmm', \sigma\sigma'} \xi \frac{1}{2} \left[j(j+1) - l(l+1) - \frac{3}{4} \right] \\ \times C_{lm, \sigma}^{jm_j} C_{lm', \sigma'}^{jm_j} f_{lm}^\dagger f_{lm' \sigma'}. \quad (51)$$

Here, Y_L are spherical harmonics, $C_{lm, \sigma}^{jm_j}$ are Clebsch-Gordan coefficients, and F^k are Slater integrals. The F^0 , the usual Hubbard U , is commonly computed by constrained LDA, while the rest of the Slater integrals (F^2 , F^4 , and F^6) are computed using atomic physics program.³² Finally, the spin-orbit strength ξ is computed within LDA program and needs to be updated during self-consistent LDA+DMFT calculation.

Exact diagonalization of the atomic Hamiltonian leads to eigenstates with conserved number of particles N , total angular momentum J , and its z component $|NJ_z; J\gamma\rangle$.

For the one-electron base, it is more convenient to choose the electron total angular momentum (j, j_z) rather than (l_z, σ), since the construction and annihilation operators conserve the z component of total spin,

$$\psi_{jj_z}^\dagger |NJ_z; J\gamma\rangle = |N+1, J_z + j_z; J' \gamma'\rangle. \quad (52)$$

Superstates $|i\rangle$ are chosen in a way to simplify the matrix elements of the creation operator ψ^\dagger . In this case, a convenient choice is

$$|i\rangle \equiv |\{NJ_z\}\rangle. \quad (53)$$

In the absence of crystal-field splitting, the hybridization Δ is a band diagonal matrix. However, strong crystal-field splitting generates off-diagonal components of $\Delta_{\{jj_z\}\{j'j'_z\}}$ and, in general, the determinant $\det(\Delta)$ in Eq. (6) cannot be broken into small determinants as in Eq. (10).

The self-energy at high frequency needs to be computed with special care in the LDA+DMFT method, since the total electronic charge in the self-consistent calculation of the electron density sensitively depends on the number of electrons in the correlated bands. It is crucial that the Green's function is compatible with the electron density computed from the local trace, namely, $n_f = T \sum_{i\omega} G_f(i\omega)$. Although some high-energy atomic states can be omitted in the Monte Carlo simulation if their probability vanishes, they cannot be neglected in computing high-frequency expansion. For practical purposes, we found it useful to compute the self-energy at high frequency from the atomlike Green's function, namely, $\Sigma(\omega \rightarrow \infty) = i\omega - E_{imp} - G^{at-1}$, where G^{at} is

$$G_{\alpha\beta}^{at} = \sum_{\{n_i\}} \frac{(F^\alpha)_{n_1 n_2} (F^{\beta\dagger})_{n_3 n_4} (P_{n_1 n_4} \delta_{n_2 n_3} + P_{n_2 n_3} \delta_{n_1 n_4})}{i\omega - E_{n_2} + E_{n_1}}. \quad (54)$$

Here, the probabilities P_{nm} are computed using Eq. (33) and the sum runs over all cluster states n_i even if their probability $P_{n_i n_i}$ vanishes. It is clear that as long as a particular cluster state m can be reached from another state n by applying creation or destruction operator and n has nonzero probability, cluster state m needs to be kept in the sum. Finally, using Eqs. (28) and (29), one can readily check that this form of self-energy gives exact first two high-frequency moments.

III. RESULTS

We implemented cellular DMFT for both the Hubbard and the t - J model on a plaquette. The energy scales are given in units of t , and Hubbard U is fixed at $12U$ while J of the t - J model is set to $J=0.3$. We simulated 5 000 000 Monte Carlo steps per processor, and results were averaged over 64 processors. One DMFT step for the Hubbard model takes approximately 45 min on 1.7 GHz personal computer processor; therefore, each Monte Carlo step requires, on average, 1×10^6 clock ticks (0.9 Mflop).

Figure 1 shows histograms (probability distribution for the perturbation order k) for few dopings of the Hubbard model $\delta=1-n$ at $T=1/200t$. The average perturbation order is increasing with doping, since the electrons are getting

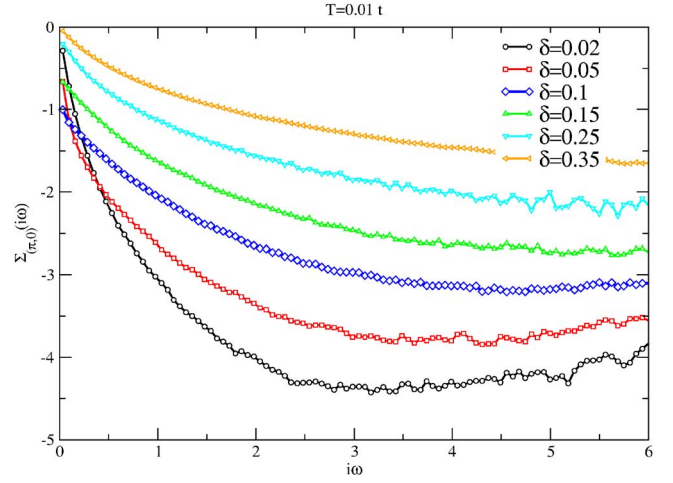


FIG. 2. (Color online) The imaginary part of the cluster self-energy $\Sigma_{(\pi,0)}$ on imaginary axis. Temperature $T=0.01t$ is around the critical temperature but still in normal state. At low frequency, the most incoherent self-energy corresponds to optimally doped and not to the underdoped system.

more delocalized (absolute value of the kinetic energy is increasing) and the creation of kinks becomes less expensive. It is of the order of 450 in overdoped regime, but the typical size of the determinant is only 112 in superconducting state or 56 in normal state.

We recently addressed the problem of coherence scale in the t - J model,³³ and we found, using NCA as the impurity solver, that the imaginary part of the cluster self-energy $\Sigma_{(\pi,0)}$, which plays the crucial role in the optical conductivity and transport, becomes very large at optimal doping and consequently the coherence scale vanishes around optimal doping. Here, we extend this study to the Hubbard model using much lower temperature. We will show that the system becomes strongly incoherent at optimal doping and the maximum of T_c tracks the maximum scattering rate in both the Hubbard and the t - J model.

Figure 2 shows the imaginary part of the self-energy $\Sigma_{(\pi,0)}(i\omega)$ at few different dopings and temperature $T=0.01t$, which is around the superconducting critical temperature of this approach. The system is still in normal state. It is clear that the self-energy at large frequencies is a monotonic function of doping and is largest at the Mott transition $\delta=0$. However, the low-frequency region is distinctly different and the crossing of self-energies is observed around $\omega_n \sim 0.1t$. Low doping as well as large doping self-energies can be extrapolated to zero, while at optimal doping, self-energy remains on the order of unity even around the critical temperature.

The upper panels of Fig. 3 show the same self-energy at small frequency for both the t - J (left) and the Hubbard (right) model. In this figure, temperature is $T=0.005t$ and is far below T_c ; therefore, all curves extrapolate to zero and the system becomes coherent in superconducting state. However, what is reminiscent of the strong incoherence at optimal doping is the large slope of imaginary part of $\Sigma(i\omega)$, which induces very small quasiparticle residue in this regime.

The precise position of the optimal doping, characterized by the largest low-frequency anomalous self-energy, is dif-

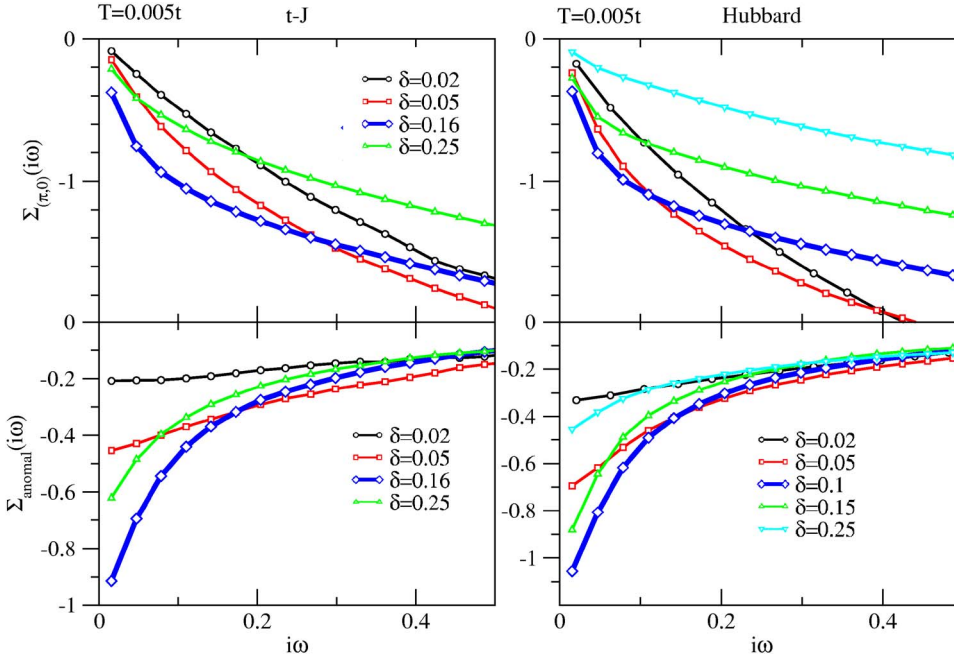


FIG. 3. (Color online) The upper panel shows the cluster $\Sigma_{(\pi,0)}$ self-energy on the imaginary axis for both the t - J (left) and Hubbard (right) model, showing the large scattering rate at optimal doping. The lower panel shows the anomalous self-energy for the same models and doping levels and can be used to locate the optimally doped regime.

ferent in the t - J and in the Hubbard model (see lower panel of Fig. 3). It is around $\delta=0.16$ in the former and around $\delta=0.1$ in the latter. However, the large scattering rate is ultimately connected with the largest anomalous self-energy and hence largest critical temperature in both the t - J and the Hubbard model.

In our view, the most important advantage of the new quantum Monte Carlo method is that it can treat the realistic multiplet structure of the atom. It was shown in Ref. 10 that the Hubbard term only (F_0) leads to severe underestimation

of the interaction strength in actinides, and for realistic values of F_0 , DMFT predicts heavy fermion state in curium rather than magnetic state. Negligence of the multiplet structure of plutonium misses the fine structure of the quasiparticles (two peaks around 0.5 and 0.85 eV) and, more importantly, predicts only weakly correlated metallic state in delta phase of plutonium.

To demonstrate the advantage of the new method, we recomputed the localization-delocalization transition in the archetype material exhibiting Kondo collapse, namely, the $\alpha \rightarrow \gamma$ transition of elemental cerium. Since the number of electrons in cerium fluctuates between states with zero, one, and two electrons in the f shell, the number of atomic states that needs to be kept is relatively small; hence, solving the impurity problem requires very little computational power in this case. In Fig. 4, we show the “valence histogram”¹⁰ of the two phases of cerium, i.e., the projection of the density matrix to the eigenstates of the atom. The plot shows the probability to find an f electron of cerium in any of the atomic eigenstates and demonstrates how strongly the atom is fluctuating between atomic states. The typical fluctuating time is inversely proportional to the Kondo temperature of the phase, being around 2000 K in the alpha phase and around 80 K in the gamma phase. The itinerant alpha-phase histogram is peaked for many atomic states, including the spin-orbit split 5/2 and 7/2 singly occupied states as well as the empty state. On the other hand, the local-moment gamma phase is peaked only at the ground state of the singly occupied sector with 5/2 spin, showing that the DMFT ground state closely resembles the atomic $N=1$ ground state.

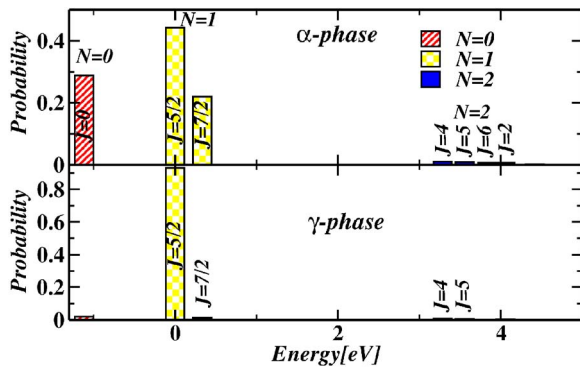


FIG. 4. (Color online) Projection of the DMFT ground state of alpha and gamma cerium to various atomic configurations of cerium atom. The histograms describe the generalized concept of valence, where the f electron in the solid spends appreciable time in a few atomic configurations. The height of the peak corresponds to the fraction of the time the f electron of the solid spends in one of the eigenstates of the atom, denoted by the total spin J of the atom. We summed up the probabilities for the atomic states, which differ only in the z component of the total spin J_z . The x axis indicates the energy of atomic eigenstates in the following way: $\text{energy}(N-1, J) = E_{\text{atom}}(N, \text{ground state}) - E_{\text{atom}}(N-1, J)$ and $\text{energy}(N+1, J) = E_{\text{atom}}(N+1, J) - E_{\text{atom}}(N, \text{ground state})$, where N is between 0 and 2.

IV. CONCLUSION

We generalized the recently developed continuous time quantum Monte Carlo expansion around the atomic limit²¹ to clusters treated within cellular DMFT or dynamical cluster

approximation as well as to materials that require realistic Hund's coupling and multiplet splitting of the atomic state. We explained the steps necessary for the efficient implementation of the method. Our low-temperature data in the strongly correlated regime of the Hubbard and t - J model show the efficiency of the method and demonstrate its superiority compared to the conventional Hirsch-Fye quantum Monte Carlo method. The long-standing problem of adequate treatment of the multiplet splitting within DMFT is resolved. This splitting is crucial in actinides, and its omission can lead to wrong prediction of the magnetic nature of the DMFT ground-state solution.

We showed that the optimality doped regime in both the t - J and the Hubbard model is characterized by the largest scattering rate and the system becomes more coherent in the underdoped and overdoped regimes. The precise position of the optimal doping, as determined from the maximum in anomalous self-energy, is different in the two models. However, the strong incoherence is always found at the doping corresponding to maximum T_c .

We computed the valence histogram across the cerium alpha to gamma transition with emphasis on the multiplet splitting of the atomic states. We showed that the atom fluctuates between many atomic states in itinerant alpha phase and both the $5/2$ and $7/2$ spin-orbit split states have large probability in the ground state of the system. The empty state and the doubly occupied states, which are substantially split by Hund's coupling, acquire a finite probability. The gamma phase, on the other hand, shows well defined valence $n_f \sim 1$, and charge fluctuations become rare.

ACKNOWLEDGMENTS

The author wishes to thank G. Kotliar for very stimulating discussion and careful reading of the paper. A fruitful discussion with C. Marianetti, O. Parcollet, P. Werner, and A. Millis is gratefully acknowledged.

APPENDIX: CELLULAR DMFT IN DIAGONAL REPRESENTATION

For the present continuous time Monte Carlo method, it is convenient to pick the base such that the local quantities are diagonal. Cellular DMFT uses generalized open boundary conditions, and therefore, in general, momentum is not a good quantum number. However, for small clusters, such as plaquette, all sites are equivalent and translational invariance is still obeyed. The local Green's function and hybridization in momentum base take the diagonal form

$$G_{cluster} = \begin{pmatrix} G_{(0,0)} & 0 & 0 & 0 \\ 0 & G_{(\pi,0)} & 0 & 0 \\ 0 & 0 & G_{(0,\pi)} & 0 \\ 0 & 0 & 0 & G_{(\pi,\pi)} \end{pmatrix}. \quad (\text{A1})$$

In superconducting state, $G_{\mathbf{k}}$ is a 2×2 matrix in Nambu notation. Although the local quantities are diagonal, noninteracting Hamiltonian at general \mathbf{k} points is not. The self-consistency condition in superconducting state takes the following form:

$$(i\omega - E_{imp} - \Sigma - \Delta)^{-1} = \sum_{\mathbf{k}} \begin{pmatrix} \xi_0(\omega) & -\phi_0(i\omega) & -iv_1 & 0 & -iv_2 & 0 & -v_0 & 0 \\ -\phi_0^\dagger(i\omega) & -\xi_0(-i\omega) & 0 & -iv_1 & 0 & -iv_2 & 0 & v_0 \\ iv_1 & 0 & \xi_1(\omega) & -\phi_1(i\omega) & v_0 & 0 & -iv_4 & 0 \\ 0 & iv_1 & -\phi_1^\dagger(i\omega) & -\xi_1(-i\omega) & 0 & -v_0 & 0 & -iv_4 \\ iv_2 & 0 & v_0 & 0 & \xi_2(i\omega) & -\phi_2(i\omega) & -iv_3 & 0 \\ 0 & iv_2 & 0 & -v_0 & -\phi_2^\dagger(i\omega) & -\xi_2(-i\omega) & 0 & -iv_3 \\ -v_0 & 0 & iv_4 & 0 & iv_3 & 0 & \xi_3(\omega) & -\phi_3(i\omega) \\ 0 & v_0 & 0 & iv_4 & 0 & iv_3 & -\phi_3^\dagger(i\omega) & -\xi_3(-i\omega) \end{pmatrix}^{-1}, \quad (\text{A2})$$

where we defined

$$v_0 = t' \sin k_x \sin k_y,$$

$$v_1 = \sin k_x (t + t' \cos k_y),$$

$$v_2 = \sin k_y (t + t' \cos k_x),$$

$$v_3 = \sin k_x (t - t' \cos k_y),$$

$$v_4 = \sin k_y (t - t' \cos k_x),$$

$$\epsilon_0 = -t(2 + \cos k_x + \cos k_y) - t'(1 + \cos k_x \cos k_y),$$

$$\epsilon_1 = t(\cos k_x - \cos k_y) + t'(1 + \cos k_x \cos k_y),$$

$$\epsilon_2 = -t(\cos k_x - \cos k_y) + t'(1 + \cos k_x \cos k_y),$$

$$\epsilon_3 = t(2 + \cos k_x + \cos k_y) - t'(1 + \cos k_x \cos k_y), \quad (\text{A3})$$

and assumed

$$\xi_0 = i\omega + \mu - (\Sigma_{11} + 2\Sigma_{12} + \Sigma_{13}) - \epsilon_0,$$

$$\xi_1 = i\omega + \mu - (\Sigma_{11} - \Sigma_{13}) - \epsilon_1,$$

$$\xi_2 = i\omega + \mu - (\Sigma_{11} - \Sigma_{13}) - \epsilon_2,$$

$$\xi_3 = i\omega + \mu - (\Sigma_{11} - 2\Sigma_{12} + \Sigma_{13}) - \epsilon_3. \quad (\text{A4})$$

Here, Σ_{11} is the normal on-site self-energy, Σ_{12} is the nearest-neighbor and Σ_{13} is the next-nearest-neighbor self-energy, and ϕ_i 's are the anomalous components of the self-energy. For d -wave symmetry, ϕ_0 and ϕ_3 vanish and $\phi_1 = -\phi_2$.

The advantage of this formulation of the cellular DMFT is that the hybridization becomes block diagonal and hence the determinants ($\det \Delta$) which enter Eq. (6) can be broken up into separate contribution for each momentum point like in Eq. (10).

-
- ¹A. Georges, G. Kotliar, W. Krauth, and M. J. Rozenberg, *Rev. Mod. Phys.* **68**, 13 (1996).
²G. Kotliar and D. Vollhardt, *Phys. Today* **57** (3), 53 (2004).
³G. Kotliar, S. Y. Savrasov, K. Haule, V. S. Oudovenko, O. Parcollet, and C. A. Marianetti, *Rev. Mod. Phys.* **78**, 865 (2006).
⁴T. Maier, M. Jarrell, T. Pruschke, and M. H. Hettler, *Rev. Mod. Phys.* **77**, 1027 (2005).
⁵G. Kotliar, S. Y. Savrasov, G. Palsson, and G. Biroli, *Phys. Rev. Lett.* **87**, 186401 (2001).
⁶S. Y. Savrasov, G. Kotliar, and E. Abrahams, *Nature (London)* **410**, 793 (2001).
⁷S. Y. Savrasov, K. Haule, and G. Kotliar, *Phys. Rev. Lett.* **96**, 036404 (2006).
⁸X. Dai, S. Y. Savrasov, G. Kotliar, A. Migliori, H. Ledbetter, and E. Abrahams, *Science* **300**, 953 (2003).
⁹K. Haule, V. Oudovenko, S. Y. Savrasov, and G. Kotliar, *Phys. Rev. Lett.* **94**, 036401 (2005).
¹⁰J. H. Shim, K. Haule, and G. Kotliar, *Nature (London)* **446**, 513 (2007).
¹¹V. S. Oudovenko, G. Palsson, K. Haule, G. Kotliar, and S. Y. Savrasov, *Phys. Rev. B* **73**, 035120 (2006).
¹²R. M. Fye and J. E. Hirsch, *Phys. Rev. B* **40**, 4780 (1989); J. E. Hirsch and R. M. Fye, *Phys. Rev. Lett.* **56**, 2521 (1986).
¹³M. J. Rozenberg, G. Moeller, and G. Kotliar, *Mod. Phys. Lett. B* **8**, 535 (1994); M. Caffarel and W. Krauth, *Phys. Rev. Lett.* **72**, 1545 (1994).
¹⁴N. E. Bickers, *Rev. Mod. Phys.* **59**, 845 (1987).
¹⁵Th. Pruschke and N. Grewe, *Z. Phys. B: Condens. Matter* **74**, 439 (1989).
¹⁶K. Haule, S. Kirchner, J. Kroha, and P. Wolfle, *Phys. Rev. B* **64**, 155111 (2001).
¹⁷H. Kajueter and G. Kotliar, *Phys. Rev. Lett.* **77**, 131 (1996).
¹⁸R. Bulla, *Phys. Rev. Lett.* **83**, 136 (1999); R. Bulla, T. A. Costi, and D. Vollhardt, *Phys. Rev. B* **64**, 045103 (2001).
¹⁹X. Dai, K. Haule, and G. Kotliar, *Phys. Rev. B* **72**, 045111 (2005).
²⁰E. Gull, P. Werner, A. J. Millis, and M. Troyer, *cond-mat/0609438* (unpublished).
²¹P. Werner, A. Comanac, L. de Medici, M. Troyer, and A. J. Millis, *Phys. Rev. Lett.* **97**, 076405 (2006).
²²P. Werner and A. J. Millis, *Phys. Rev. B* **74**, 155107 (2006).
²³P. Werner and A. J. Millis, *Phys. Rev. B* **75**, 085108 (2007).
²⁴C. A. Marianetti, O. Parcollet, K. Haule, and G. Kotliar, *cond-mat/0612606* (unpublished).
²⁵J. C. Slater, *Phys. Rev.* **165**, 655 (1968).
²⁶A. N. Rubtsov, V. V. Savkin, and A. I. Lichtenstein, *Phys. Rev. B* **72**, 035122 (2005).
²⁷J. Kroha, P. Wölfle, and T. A. Costi, *Phys. Rev. Lett.* **79**, 261 (1997).
²⁸G. Yuval and P. W. Anderson, *Phys. Rev. B* **1**, 1522 (1970).
²⁹F. D. M. Haldane, *Phys. Rev. Lett.* **40**, 416 (1978); *J. Phys. C* **11**, 5015 (1978).
³⁰Q. Si and G. Kotliar, *Phys. Rev. B* **48**, 13881 (1993).
³¹A. Schiller, F. B. Anders, and D. L. Cox, *Phys. Rev. Lett.* **81**, 3235 (1998).
³²R. D. Cowan, *The Theory of Atomic Structure and Spectra* (University of California Press, Berkeley, 1981).
³³K. Haule and G. Kotliar, *cond-mat/0605149* (unpublished).